Korean J. Chem. Eng., **31**(12), 2136-2144 (2014)
DOI: 10.1007/s11814-014-0164-6

pISSN: 0256-1115
eISSN: 1975-7220

Modeling and analysis of a syngas cooler with concentric evaporator channels in a coal gasification process

Junho Oh*, In-Soo Ye*, Sangbin Park*, Changkook Ryu*,†, and Sung Ku Park**

*School of Mechanical Engineering, Sungkyunkwan University, Suwon 440-746, Korea
**Coal Conversion System Development Team, Corporate R&D Institute,
Doosan Heavy Industries & Construction, Daejeon 305-811, Korea
(*Received 6 April 2014 • accepted 12 June 2014*)

Abstract−Coal gasification offers a flexible and efficient conversion of the solid fuel into CO- and H_2-rich synthetic gas (syngas) for production of various chemicals and energy products. Since the hot syngas leaving a gasifier contains various impurities such as acidic gases and particulates, it needs to be cooled down for cleaning prior to conversion into the final product. A dedicated heat exchanger called a syngas cooler (SGC) is used to lower the gas temperature while recovering the thermal energy. This study investigated the heat transfer characteristics in a commercial-scale SGC consisting of a series of concentric helical coil channels. First, the detailed flow and heat transfer pattern in the unique heat exchanger were analyzed using computational fluid dynamics (CFD) for various operating loads and fouling conditions. The predicted heat transfer rate was used to derive correlations for Nusselt number for the channel sections of the SGC. Second, a one-dimensional model of the equipment was proposed for fast-response process simulations. In terms of heat transfer rate and gas temperature, the process model showed a reasonable accuracy compared to the CFD results for the tested cases.

Keywords: Coal Gasification, Heat Exchanger, Helical Coil Channel, Process Model, Syngas Cooler

INTRODUCTION

Gasification of coal converts the carbonaceous solid fuel into CO and H_2-rich syngas using air, oxygen and/or H_2O. The syngas can be then used to produce a wide range of chemicals and energy products such as H_2, CH_4, ammonia/urea, methanol and electricity. For generation of electricity, the integrated gasification combined cycle (IGCC) has been applied in the industry [1]. The integrated gasification fuel cell (IGFC) combined with CO_2 capture is drawing attention as an alternative technology for the future. The total worldwide capacity of IGCC plants using coals as the primary feedstock is about 70,000 MW_{th} as of August 2013. This figure is expected to be doubled in 2015 based on data of gasifiers under construction, and tripled in 2018 based on planning [2].

Among the various reactor configurations, entrained flow gasifiers are commonly used in commercial plants [3]. They typically operate at a high temperature (~1,500 °C at the exit) and high pressure (20-60 bar). During coal gasification, the sulfur, nitrogen and mineral matter in coal are also released as various impurities in the syngas in the form of H_2S, HCN, molten ash (slag) etc. These impurities should be removed from the syngas before it undergoes the final energy production or chemical conversion process. First, the raw syngas at the exit of the gasifier requires immediate quenching to below the melting temperature of the ash to prevent slag deposition. In various commercial processes using entrained flow gasifiers, the syngas is quenched by water spray (water quench), recycled cold syngas (gas quench), or endothermic gasification reactions (chemical quench) [4-7]. The raw syngas is further cooled down in a syngas cooler to about 200-300 °C to prepare it for a series of cleaning processes downstream. This cool down is achieved by a heat exchanger (syngas cooler, SGC) which recovers the thermal energy in the syngas as steam, or simply by total water quenching at a lower efficiency.

A SGC, if used, is configured differently from conventional heat exchangers. Operating at a high pressure, it has to handle highly concentrated fly slag particles whose the impaction and deposition may lead into a blockage, erosion, fouling and/or corrosion in the equipment. Therefore, SGC has simple passes for gas flow to minimize particle impaction. One example of SGC is the radiant syngas cooler (RSC) adopted in GE Energy's processes [8]. Installed at the bottom of a down-fired gasifier, the RSC has a simple internal structure consisting of membrane water-walls with a water-quenched slag tap at its bottom. An RSC can be combined with a convective heat exchanger downstream. Several experimental and numerical studies have been conducted for flow patterns of gas and particles in this type of SGC [4,9,10]. The SGC adopted in Shell coal gasification processes consists of a series of concentric heat exchangers made of helical coil tubes. After quenching the syngas at the top of the gasifier to about 900 °C, the syngas enters the SGC where it splits into long vertical channels separated by helical coil tubes. The key phenomena in the gas quench process and in the entry section of the SGC have been recently reported by the authors [11,12]. Similar heat exchangers made with helical coils have been studied for heat transfer [13-15], but the actual configuration used in the SGC is different from those in terms of the shape, size and operating conditions. For efficient design and operation of the SGC at various scales

†To whom correspondence should be addressed.
E-mail: cryu@skku.ac.kr
Copyright by The Korean Institute of Chemical Engineers.

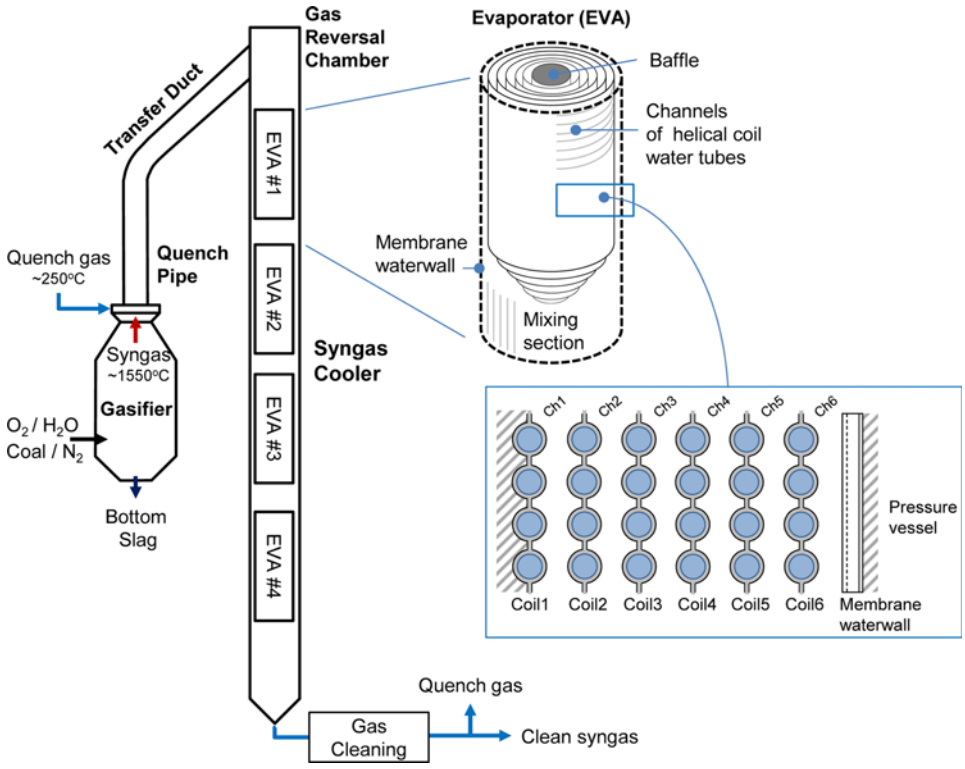

Fig. 1. Schematic of the syngas cooler in the gasification block of an IGCC process.

or operating conditions, fundamental understanding is required on the flow and heat transfer characteristics within the heat exchanger.

This study investigates the flow and heat transfer characteristics in a SGC with multi-staged evaporators of a commercial IGCC process for various operational loads and fouling conditions. The first step of investigation was conducted using a commercial CFD code for detailed gas flow and heat transfer rates in the channel and mixing sections of heat exchangers in the SGC. Based on the results, a correlation for convective heat transfer was derived. Second, a process model for the SGC incorporating the convection correlation was constructed to use in fast-response simulations for design and operation diagnostics of the whole process. The reliability of the simplified model was evaluated for local and overall heat transfer characteristics by comparison of the results with the CFD results.

NUMERICAL METHODS

1. Process Description for SGC

Fig. 1 shows a process diagram of a gasification block applied for a commercial IGCC plant at 300 MWe capacity. The syngas produced in the gasifier has a temperature of approximately 1,550 °C that is immediately quenched in the quench pipe to about 900 °C by mixing with the cold syngas recycled from downstream. Through the transfer duct, the syngas is transported to the SGC. In the upper part of the SGC, the syngas flow rapidly turns downward to enter the heat exchanger sections. This part is called the gas reversing chamber (GRC). The detailed flow and heat transfer characteristics for the quench pipe/transfer duct and GRC have been previously reported [11,12].

The SGC consists of membrane water-walls aligned vertically,

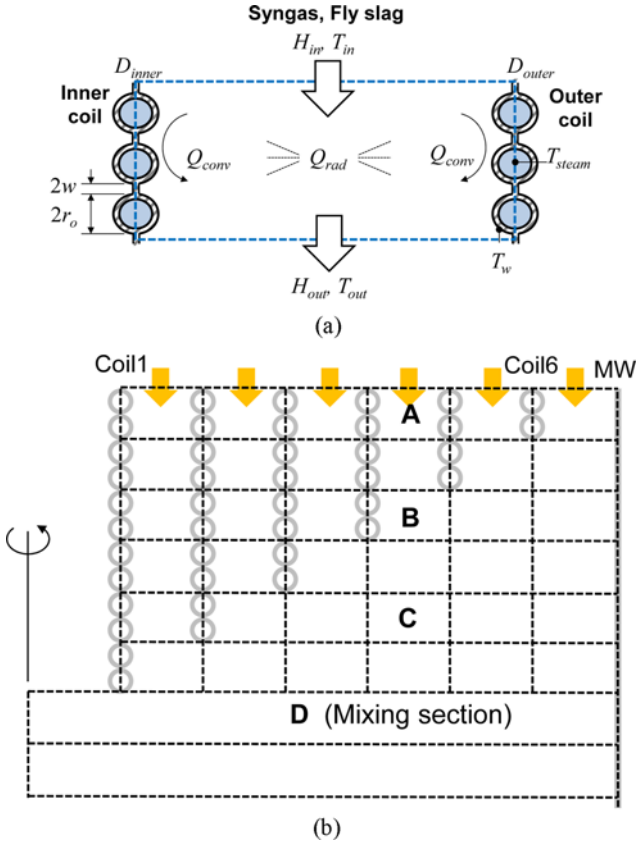

Fig. 2. Schematic of the modeling approach for the SGC in the process model.
(a) Control volume in a channel, (b) Structure of control volumes in the lower part of EVA1

Table 1. Operating conditions for the SGC for three loads

	Load		50%	75%	100%
Inlet conditions	Syngas	Flow rate (kg/s)	56.6	84.8	113.1
		Temperature (°C)	670.8	721.7	740.0
		CO (vol%)	55.2	57.2	59.2
		CO_2 (vol%)	7.2	6.1	5.1
		H_2 (vol%)	27.2	28.2	28.5
		N_2 (vol%)	10.4	8.5	7.2
	Coal ash	Flow (kg/s)	0.66	1.00	1.32
	Flux	Flow (kg/s)	0.26	0.38	0.52
Fouling factor, R_{foul} ($K \cdot m^2/W$)			0 (clean), 6.3×10^{-4}, 12.5×10^{-4}		

forming a very tall cylinder. It is about 74 m tall including the GRC with a diameter of about 2 m. It incorporates four evaporator (EVA) sections inside, each with a length of about 10 m. The first three EVAs (1-3) are for high-pressure (HP) steam at about 150 bar (T_{sat}= 340 °C), and EVA4 for medium-pressure (MP) steam of about 55 bar (T_{sat}=270 °C). Each EVA has long concentric channels made of numerous helical coil water tubes, as depicted in Fig. 2. Since the tubes are welded by fins, the welded are completely isolated from each other. EVA1 has six channels, including the one between the outermost coil (Coil 6) and the membrane wall. Each channel is numbered from 1 to 6 outwards, as indicated in the figure. In EVA2 and EVA3, coil 1 and channel 1 are removed to increase the gas velocity. In EVA4, coil 2 and channel 2 are also removed to have four outer channels. The central part of the EVAs is blocked by a baffle at the top and, therefore, no flow enters this part. At the end of the channels, the syngas flows from the channels gather into a hollow mixing section before it enters the next EVA.

Table 1 lists the operating conditions of the SGC considered in this study for three operational loads of 50, 75 and 100%. The operating pressure was fixed at 42 bar, gauge. The conditions for the flow rate and the compositions of syngas, coal and flux are based on the design values, which have been detailed in previous studies for the quench pipe/transfer duct [11] and for the GRC [12]. The coal and flux particles had particle diameters ranging from 2-67 μm and 4-105 μm, respectively. The temperature at the inlet was derived from the average value at the outlet of the GRC predicted using the CFD.

In addition to the effect of the operational load, the effect of fouling on heat transfer was investigated for two fouling factors: 6.3×10^{-4} and 12.5×10^{-4} $m^2 \cdot K/W$. This was to consider the formation of fouling layer by the accumulation of fly slag particles onto the tube surfaces. Assuming a thermal conductivity of the fouling layer to be at 1.595 $W/m^2 \cdot K$ [16], this corresponded to a thickness of 1 and 2 mm, respectively.

2. Methods of Computational Fluid Dynamics

Since the SGC consisted of thousands of small tubes in a long cylinder, each EVA was modelled consecutively, and the results of CFD were used to determine the inlet condition for the next one. Due to the membrane waterwall oriented vertically, a 2-dimensional axisymmetric mesh was not appropriate. Therefore, the mesh was constructed for a single fin-tube unit of the membrane wall, which was about 1.3° of the cross-section, with the symmetric condition for both sides. A total of approximately 1.8, 2.0, and 2.1 million hexahedral cells were used for EVA1, EVA3 and EVA4, respectively. The mesh for EVA2 was also used for EVA3 because they both had identical geometry. The detailed image of the mesh is provided in Fig. S1 of the Supplementary Information. Note that the mesh included the solid zone of the tubes, while the water/steam section inside the tubes was treated as walls with convection.

The gas flow in the SGC can be considered as particle-laden turbulent flow. The general approach for CFD was identical to that for the upstream equipment [11,12], and therefore, it is briefly described herein. The Lagrangian scheme was applied to track individual particles to determine their exchange of momentum and heat transfer with the gas phase and the walls. The particles had a fixed density of 2,800 kg/m^3 and emissivity of 0.83 [17]. The emission and absorption by the particles were calculated based on the cumulative cross-sectional area of the particles within a cell volume, which had 20 size fractions in total within the range given in Table 1. The turbulence was solved by the realizable k-ε model [18], which has a more fundamental foundation for jet and circulating flows. The model was found the most appropriate for simulations in a RSC [10]. The radiation was predicted by the discrete ordinate method with an angular discretization of five divisions and three pixels both in the polar and azimuthal directions. The absorption coefficient was calculated using the weighted sum of the gray gases model (WSGGM) with the model coefficients proposed by Smith et al. [19]. The coefficients are valid up to 10 bar·m. Although the operating pressure of the SGC was very high (43 bar), the partial pressures of CO_2 and H_2O (about 3.0 and 0.1 bar, respectively) were within the valid range. Due to the high concentration of particles, however, the absorption coefficient of the particles was dominant over that of the syngas. For example, the volume-average value was about 2.9 m^{-1} for the particles and about 31 m^{-1} for the gas in EVA1 at 100% load.

Regarding the boundary conditions, the inner surface of the water tubes had a convection coefficient of 1×10^4 $W/m^2 \cdot K$, considering the phase change with a temperature fixed to the saturation value (340 °C for EVA1-3 and 270 °C for EVA4). The outer surface of the SGC wall was assumed adiabatic, since it faced an enclosure of a pressurized vessel filled with the steam. For the innermost coils, the surface facing the central part of the SGC was also assumed adiabatic, which was filled with stagnant syngas. The emissivity of the entire walls was assumed to be 0.8, considering the highly corrosive conditions. The thermal conductivity (k_{tube}) of the tube materials was expressed into a polynomial of temperature, which was about 17 W/m·K for EVA1-3 and 40 W/m·K for EVA4 at the saturation temperature of the water. The CFD simulations were conducted using

ANSYS FLUENT version 13 [20]. Although the results of this study are not directly validated by operation data, the use of CFD for a helical coil heat exchanger has been proven to have a reasonable agreement with experiments [14,15].

3. Development of the Process Model

Fast-response process simulations are used in design and operation diagnostics for various conditions in different processes including gasification. Instead of rigorous CFD simulations, such model can quickly provide the overall heat transfer and gas temperatures for key parts of a process. The modeling approach is described as follows.

In the process model, the helical coil tubes are simplified as a smooth cylinder. Also, it is assumed that the mass flux is uniform between the channels of an EVA. The actual distribution of mass within the channels will be discussed later with the CFD results. Then, a control volume for a small horizontal part of each channel or in a mixing section is illustrated as in Fig. 2(a). For each control volume, the energy balance can be expressed by the following simple conservation equation:

$$H_{g,in}=H_{p,in}=H_{g,out}+H_{p,out}+Q_{conv}+Q_{rad} \tag{1}$$

The enthalpy of the gas or the particle phase (H_j) at the inlet/outlet of the control volume depends on the temperature, as follows.

$$H_j = M_j\int_{T_{ref}}^{T_j} C_{p,j}dT \tag{2}$$

The temperature at the outlet of a control volume became the unknown to be determined from Eq. (1). The mass flow rate in a channel was calculated as the mass flux multiplied by the cross-sectional area of a channel. The convection heat transfer to the wall was determined by the temperature difference of the syngas and the water/steam and the convection coefficient (h_g), as follows.

$$Q_{conv}=h_{conv}A_w(T_{avg}-T_w) \tag{3}$$

T_{avg} represents the average temperature in the control volume as follows.

$$T_{avg}=(T_{in}+T_{out})/2 \tag{4}$$

The convection coefficient was calculated by a correlation of Nu.

$$h_{conv}=\frac{Nu\cdot k_g}{D_h} \tag{5}$$

D_h is the hydraulic diameter equivalent to the spacing between the outer and inner coils of the concentric channel, ($D_h=D_{outer}-D_{inner}$). Since the configuration of helical coil tubes in the SGC was not common, a correlation to be readily adopted to the model was not available in the literature. Therefore, Nu was expressed in the following simplest form and the coefficients, C and m, were derived from the CFD results.

$$Nu=C\cdot Re^m\cdot Pr^n \tag{6}$$

The exponent n for Pr was fixed constant at 1/3. In the radiative heat transfer, it was assumed that the gas exchanges radiation with the walls within the control volume, ignoring the exchange between adjacent ones. The radiation from the gas and particles to the wall was calculated by the following simple equation, which was based on a gray body within a sufficiently long enclosure.

$$Q_{rad}=\frac{\sigma A_w(T_{avg}^4-T_w^4)}{\frac{1}{\varepsilon_{CV}}+\frac{1}{\varepsilon_w}-1} \tag{7}$$

In Eq. (7), ε_{CV} incorporated the contributions of the gas and particles. Since the emission of the particles was dominant over that of the gas, ε_{CV} was calculated using the particle concentration and size distribution as described in [11].

Eqs. (3) and (7) involve T_w, which is not uniform along the tube and fin surfaces. In the model, T_w was assumed to be uniform so that it can be determined by the heat balance together with T_{out}. First, the total heat transfer from the gas to the steam can be represented by using the overall heat transfer coefficient, as follows.

$$Q_{steam}=Q_{rad}+Q_{conv}=U_{gas\text{-}steam}A_w(T_{avg}-T_{steam}) \tag{8}$$

The overall heat transfer coefficient ($U_{gas\text{-}steam}$) in Eq. (8) includes the thermal resistance by the convection and radiation from the gas side, the conduction through the fouling layer and the tube, and the convection by the water/steam inside. Detailed analytical study on $U_{gas\text{-}steam}$ has been presented by Bowen et al. [21] using the steady-state thermal resistance approach for membrane waterwall tubes in which one side is insulated. For the helical coils of the SGC, however, both sides face the heat influx from the inner and outer channels. Therefore, the centerline of the tube can be considered as an adiabatic boundary. This simplifies $U_{gas\text{-}steam}$ by Bowen et al.'s second method into the following equation.

$$U_{gas\text{-}steam}=\frac{\pi/(2r_o+2w)}{1/h_{steam}r_i+\ln(r_o/r_i)/k_{tube}+R_{foul}+1/(h_{conv}+h_{rad})} \tag{9}$$

The thermal resistance in the fin was assumed to be negligible in Eq. (9), which shrinks the equation identical to that for a cylindrical tube over a distance of $2(r_o+w)$. A separate numerical study on the coil geometry summarized in the Supplementary Information showed that $U_{gas\text{-}steam}A_w$ calculated by Eq. (9) had errors smaller than 1.7%. It was also found that the predicted values were within 3.2% of those for the membrane wall with an adiabatic boundary on one side. Therefore, Eq. (9) was also applied both to the innermost coil and the membrane waterwall, which can significantly simplify the solution procedure. To determine T_w, Eqs. (8) and (9) were expressed for the heat transfer from the outer tube surface to the water/steam, as follows:

$$T_w=\frac{Q_{rad}+Q_{conv}}{U_{w\text{-}steam}A_w}+T_{steam} \tag{10}$$

$$U_{w\text{-}steam}=\frac{\pi/(2r_o+2w)}{1/h_{steam}r_i+\ln(r_o/r_i)/k_{tube}+R_{foul}} \tag{11}$$

$$A_w=\pi(D_{inner}+D_{outer})\Delta y \tag{12}$$

The above equations have two main unknowns, T_{out} and T_w, which were solved iteratively. In each control volume, Q_{rad} and Q_{conv} were initially calculated with T_{in} taken as T_{avg}. Then, T_w was calculated using Eq. (10), and T_{out} using Eq. (1) iterated by the Newton-Raphson method. With an updated value of T_{avg} from Eq. (4), the calculations were repeated until the change in T_{out} become less than 0.01 °C.

Fig. 2(b) illustrates the structure of control volumes in the lower part of EVA1 in which the channels end and the mixing section starts. The solution procedure for a control volume was continued by marching from the top to the bottom of control volumes in each channel

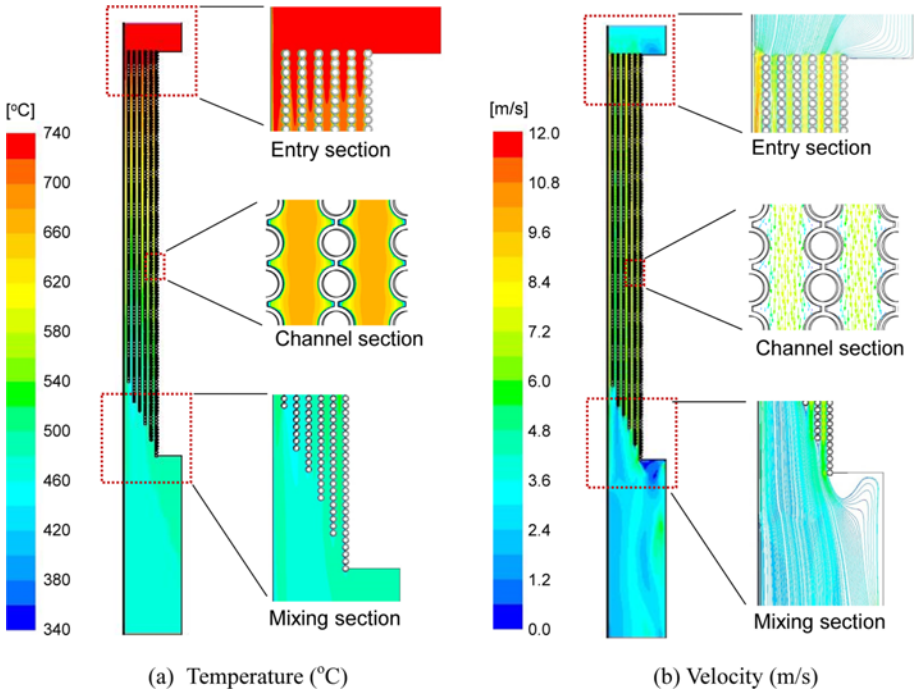

Fig. 3. CFD results of temperature and velocity in EVA1 at load 100%.

of an EVA. For the wall surface area for heat transfer (A_w), Eq. (12) was applied the control volumes within a channel such as the one indicated as 'A' in the figure. If the outer coil ended in the control volume 'B', A_w was only calculated for the inner coil. A_w became zero in the control volume 'C', and the gas temperature did not change since the heat exchange between adjacent control volumes was not considered. Once the calculations for the channels section were over, the gas temperatures from the six channels were mass-averaged to determine T_{in} for the first control volume of the mixing section ('D'). Then, the calculation was repeated to the next EVA.

The solution procedure was developed into a program using Microsoft Excel Visual Basic. The models for the physical properties of the gas and the particles were identical to those used in the CFD. The number of control volumes was 100 along the channel and mixing sections of a channel in each EVA. With the implicit scheme used in the calculation, the grid sensitivity was minimal. For example, the temperature changes were less than 0.1% compared to the results for 200 control volumes each. Due to the simple procedure, the calculation for the four EVAs took less than one second on a PC with an Intel i5-3570 processor.

RESULTS AND DISCUSSION

1. Gas Flow Characteristics

Fig. 3 illustrates the contour of the velocity and temperature in EVA1 at load 100% with no fouling. In the entry region (Fig. 3(a)), the gas flow was more concentrated in the outermost channel than in the inner channels. This was because the resistance to the flow was lower by the orientation of the water tubes in the wall parallel to the gas flow. Also, the length of the channel was the shortest which reduced the pressure drop compared to the inner channels. Within the channels, the gas mainly flowed along the center, although it became stagnant in the region near the fins between the curved tubes. Due to the low gas velocity, small fly slag particles were likely to accumulate more onto the surface near the fins than onto the circular section facing the strong gas flow. The gas temperature and velocity gradually decreased by the heat transfer to the water/steam inside the tubes. However, the temperature was higher in the outermost channel, due to the relatively larger mass flow rate. At the end of the channels, the gas from the channels entered a mixing section. A large circulation zone was formed in the central part below the channels, since the volume above (the internal part enclosed by coil 1) was blocked by the baffle on the top. Since the mixing region

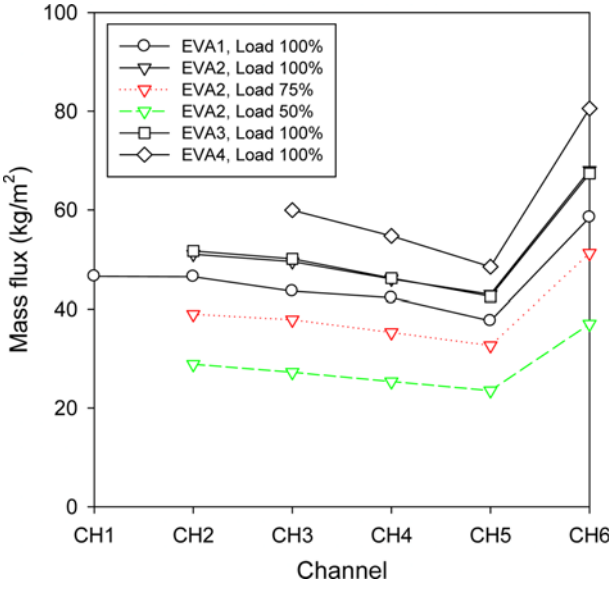

Fig. 4. Comparison of mass flux at each channel of the evaporators.

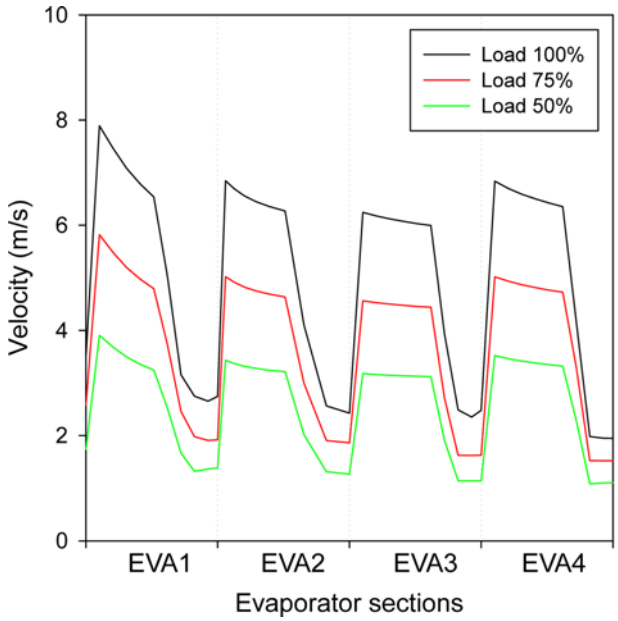

Fig. 5. Profiles of gas velocity along the evaporator sections for different operational loads.

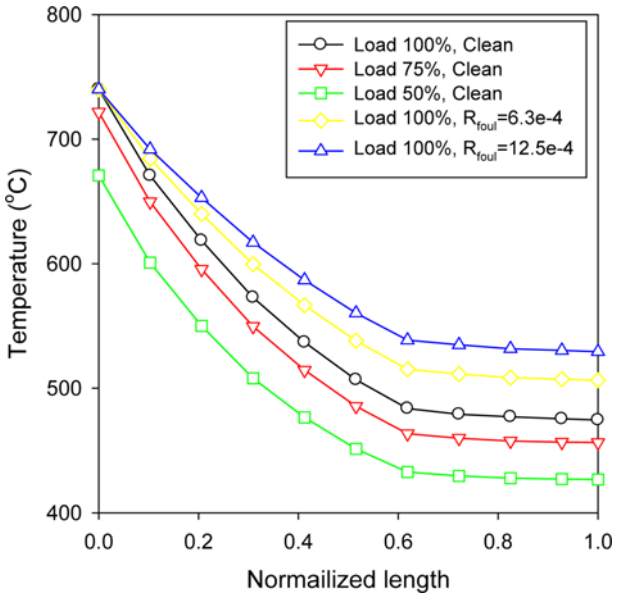

Fig. 6. Profiles of average temperature in HP EVA1 predicted by CFD for different loads and fouling conditions.

was about 4 m high, the gas flow became uniform as it approached EVA2. Similar flow patterns were repeated in other EVAs although the length and number of channels were different. Therefore, the results are presented using the profiles of average temperature, heat flux and other key parameters.

Fig. 4 presents the mass flux at each channel of the evaporators. Channel 1 was removed from EVA2, and channel 2 was also removed in EVA4 to increase the gas velocity and reduce the construction costs. The mass flux consistently had the largest values in the outermost channels, but the least in channel 5 had the least. When the cross-sectional area was multiplied to the mass flux, channel 6 represented 26.0% of the total flow rate in EVA1 and 36.2% in EVA4.

Fig. 5 shows the profiles of mass-weighted average velocity along the length of the SGC for different operational loads without fouling. The plateaus and dips of the velocity indicate the channel and mixing sections of the four EVAs, respectively. For the operational load of 100%, the gas velocity was the highest (about 8 m/s) at the entry of EVA1 and gradually decreased within the channels as the gas temperature decreased. In the mixing zone, the velocity was below 3 m/s. The velocity at the entry of EVA2 was higher than that at the exit of the EVA1 channels since channel 1 was blocked. A similar increase in the gas velocity was observed in EVA4 in which two inner channels were removed. Overall, the velocity within the channels was maintained within a range of 3-8 m/s, which appeared to be appropriate. A faster velocity may erode the tube surfaces due to the impact of fly slag particles [12]. On the other hand, a low velocity may increase the deposition of the particles within the channels, especially under low operational loads, seriously fouling the surfaces and thereby deteriorating the heat transfer efficiency. If severe, the deposition may also block parts of the channels. Reducing the number of channels in the downstream heat exchangers was crucial in maintaining sufficiently high gas velocities.

2. Heat Transfer Characteristics

Fig. 6 plots the profiles of the enthalpy-averaged temperature along the length of EVA1 for different operational loads and fouling conditions. The temperature rapidly decreased in the channel section, for example from 740 °C to 479 °C at 100% load without fouling. In the mixing section, the temperature decreased by less than 5 °C, since the heat transfer surface was limited to the membrane wall of the SGC. When fouling was considered, the gas temperature at the exit was increased to 504 °C for of R_{foul}=6.3×10^{-4} K·m^2/W and to 527 °C for 12.5×10^{-4} K·m^2/W. This corresponded to 12% and 20% of decrease in the heat transfer rate, respectively. The trends of the temperature in the rest of the EVAs are presented later with the results from the process model.

Fig. 7 plots the average heat flux in the channel and mixing sec-

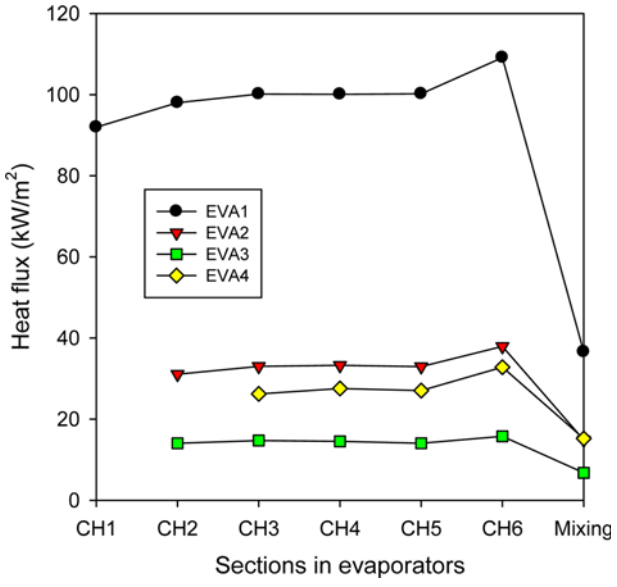

Fig. 7. Heat flux in the channels and mixing sections of evaporators predicted by CFD for different loads and fouling conditions.

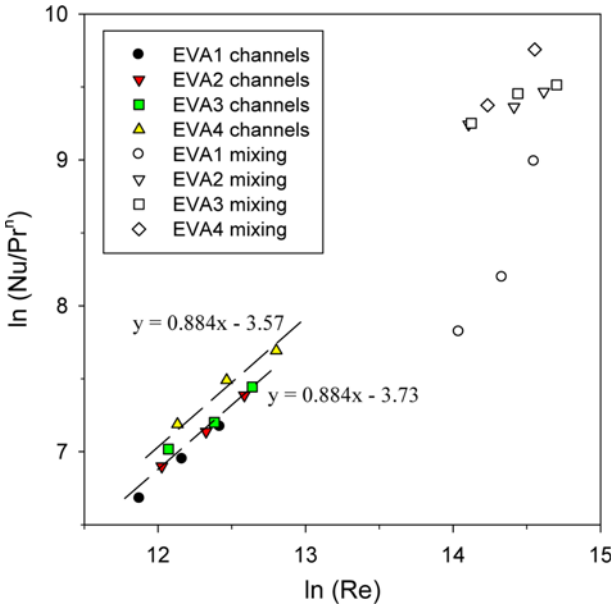

Fig. 8. Linear regression of ln(Re) vs. ln(Nu/Pr^n) predicted for the average values in the channels and mixing sections of the evaporators.

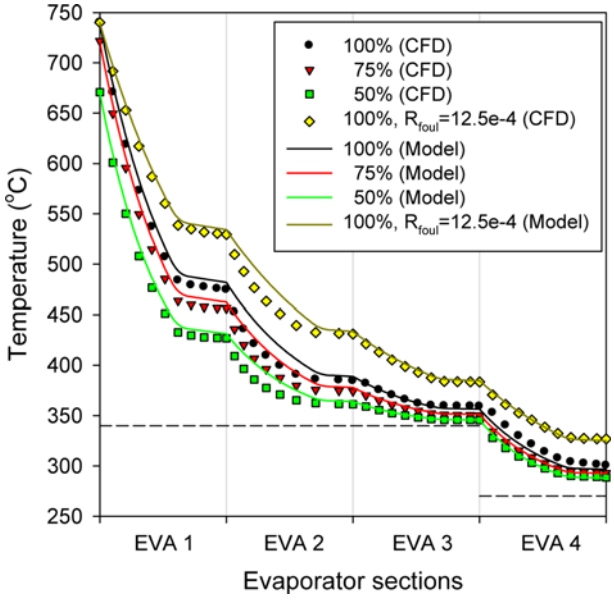

Fig. 9. Comparison of temperature profiles in the entire SGC predicted by CFD and the process model.

tions of each evaporator. The heat flux decreased from 98.1 kW/m^2 in EVA1 to 33.2 kW/m^2 in EVA2 and further down to 14.4 kW/m^2 in EVA3. This was mainly because the temperature difference between the gas and the water/steam in the tubes became smaller along the length. The lowered gas temperature also reduced the velocity and corresponding convection as well as the radiation from the fly slag particles. The heat flux slightly increased in EVA4 for two reasons. First, the saturated temperature of the water/steam was lower (270 °C) than that of the earlier evaporators (340 °C). Second, the gas velocity was increased by the removal of two inner channels. The mixing sections of the evaporators had heat flux of about 7.0-36.6 kW/m^2. However, the contribution of the mixing sections to the total heat transfer rate was not significant (2.5%-11.6% of the total), since the heat was absorbed only on the membrane wall.

For the convective heat transfer and the average gas temperature predicted in each section, the convection coefficient (h_g) was evaluated to derive the correlation of Nu required for the process model. Fig. 8 plots ln(Re) vs. ln(Nu/Pr^n) for the channels and mixing sections of the evaporators under operational loads of 50-100%. EVA4 had slightly higher values of Nu compared to the EVAs above. This was due to the difference caused by the significantly higher thermal conductivity of tube materials (about 40 W/m·K for EVA4 and 17 W/m·K for the rest). The mixing sections had higher Nu and Re than the channel sections simply due to its larger characteristic length (the SGC diameter of about 2.0 m). For the channel sections of EVA1-3 for HP steam, the results were grouped together and fitted to a single linear equation: ln(Nu/Pr^n)=0.884 ln(Re)–3.73. The result for the channel zone of EVA4 for MP steam was fitted to another equation: ln(Nu/Pr^n)=0.884 ln(Re)–3.57, maintaining the sample slope. With the exponent of Pr of 1/3, the resultant correlations of Nu became as follows:

- EVA1 to EVA3 for HP steam,

$Nu=0.024Re^{0.884}Pr^{1/3}$ (Re: 1.4×10^5-3.1×10^5, Pr: 0.832-0.849)

- EVA4 for MP steam,

$Nu=0.028Re^{0.884}Pr^{1/3}$ (Re: 1.9×10^5-3.6×10^5, Pr: 0.850-0.855)

The above two correlations were introduced to the process model for calculation of convection. For the mixing zone, correlations were not derived since the data points were not deviated far from the extrapolation of the correlations for the mixing zone except for the EVA1 mixing section. Despite the deviations from the correlation, the heat transfer rate in the mixing zone had little significance due to the small proportion of to the membrane wall in the total surface area.

3. Comparison of CFD and Process Model

Fig. 9 compares the average temperatures predicted by CFD and by the process model in the entire system for selected cases. The differences in heat transfer between the channels and mixing sections of EVAs can be easily recognized in the temperature profiles. The channels section of EVA1 had the largest decrease in temperature while EVA3 had the least. Under the fouling-free condition, the temperature difference in EVA3 was only about 16-25 °C for load 50-100%, representing about 4.7-6.5% of the heat absorbed in the first three EVAs for HP steam. With R_{foul} of 12.5×10^4 K·m^2/W (equivalent to 2-mm-thick fouling layer), however, the temperature drop in EVA3 became 28-47%. The proportion of heat absorption in EVA was also approximately doubled (8.8 to 12.8%). Compared to EVA3, EVA4 had larger temperature drops due to the decrease in the water/steam temperature.

The temperatures predicted by the process model are plotted as solid lines in Fig. 9. Overall, the temperature trends were reasonably predicted by the model in the different sections of EVAs. The largest discrepancy between the two models was about 21 °C, which mainly occurred in EVA2. Considering the trend between the two results, the correlation of Nu in the process model underestimated the convection in the thermal entry region of the channels in EVA2. The difference between the models was reduced to below 10 °C as the gas approached the mixing section.

Table 2. Summary of the results from CFD and the process model for the SGC

Load		100%	75%	50%	100%	75%	50%
R_{foul} ($K \cdot m^2/W$)			0			12.5×10^{-4}	
T_{in} (°C)		740.0	721.7	670.8	740.0	721.7	670.8
EVA 1-3 (HP)	$T_{out, CFD}$ (°C)	359.3	350.5	345.6	383.5	370.3	356.9
	ΔT	−2.8	0.8	0.2	1.3	−0.7	−2.4
	Q_{CFD} (MW_{th})	66.3	48.1	27.6	62.2	45.6	26.7
	$\Delta Q/Q_{CFD}$	0.7%	−0.2%	−0.0%	−0.3%	0.2%	0.7%
EVA4 (MP)	$T_{out, CFD}$ (°C)	300.4	292.9	288.6	326.8	315.5	303.8
	ΔT	−3.7	−0.4	−0.6	−1.9	−3.5	−4.6
	Q_{CFD} (MW_{th})	9.8	7.2	4.7	9.5	6.8	4.3
	$\Delta Q/Q_{CFD}$	1.5%	2.2%	1.4%	5.5%	5.1%	3.9%

$\Delta T = T_{out, PM} - T_{out, CFD}$, $\Delta Q = Q_{PM} - Q_{CFD}$, PM: process model

The amount of heat transfer and the discrepancies between the two models are summarized in Table 2. In the results predicted by CFD, the total heat transfer rate in the SGC was 76.1 MW_{th} for 100% load and 32.2 MW_{th} for 50% load under the clean surface condition. The first three EVAs absorbed 86-87% of the total heat regardless of the load and fouling conditions. Radiation predicted by the CFD accounted for 12.6-14.1% of the total on the clean surfaces and 17.5-19.1% for R_{foul} of 12.5×10^4 $K \cdot m^2/W$. Overall, the results from the process model agreed reasonably well with the CFD for different loads and fouling conditions. The largest deviation was found in the EVA4 with fouling, in which the process model overpredicted heat transfer by 5.5% (0.52 MW_{th}) and the corresponding exit temperature was 4.6 °C lower. The deviations were much smaller for the clean surface conditions. Since the performance of the process model was overall satisfactory, it can be used to predict the temperature and heat transfer profiles along the exceptionally tall equipment for various conditions. Further elaboration and validation of the model are also essential for different pressures, syngas compositions and changes in the arrangement or dimensions of the EVAs.

CONCLUSIONS

The flow and heat transfer characteristics in the SGC of a commercial IGCC process were investigated using CFD. Based on the results, a one-dimensional process model was established to provide a fast-response process simulation of the equipment.

The flow characteristics of syngas were different between the channel section and mixing section of an EVA. The concentric channel sections made of helical coil tubes had higher gas velocities and larger heat transfer rates than the mixing section. For operational loads between 50-100%, the gas velocity was maintained between 3-8 m/s in the channel section by removing inner channels in the downstream EVA. Among the channels of an EVA, the largest proportion of the syngas flow was induced to the outermost one of which the length was the shortest and the membrane waterwall was oriented parallel to the gas flow. The larger mass flux within this channel also led to larger heat flux than that of other channels in all EVAs.

In the four EVAs of the SGC, the total heat transfer rate ranged from 32.3 to 76.1 MW_{th} with an exit temperature of 280-300 °C for loads between 50-100% without fouling. The heat was absorbed mostly in the first EVA where the temperature difference between the syngas and the water/steam was the largest. The fouling factor of 12.5×10^4 $m^2 \cdot K/W$ reduced the heat transfer rate by up to 6.8%. Using the CFD results, the correlations of Nu were derived for the convection heat transfer in the channel sections.

Despite the simplifications on the mass distribution and heat transfer, the process model for the SGC predicted the heat transfer rate and corresponding gas temperature that were in good agreement with the CFD results. The maximum difference between results of the two models was 5.5% for the heat transfer rate and −4.6 °C for the exit temperature.

ACKNOWLEDGEMENTS

This work was supported by the New & Renewable Energy Core Technology Program of the Korea Institute of Energy Technology Evaluation and Planning (KETEP) and Doosan Heavy Industries and Construction granted financial resource from the Ministry of Trade, Industry & Energy, Republic of Korea (2011951010001A).

NOMENCLATURE

A : area [m^2]
C : model constant for Nu
C_p : specific heat [$J\ kg^{-1}\ K^{-1}$]
D : coil diameter, hydraulic diameter [m]
h : convection coefficient [$W\ m^{-2}\ K^{-1}$]
H : total enthalpy [$J\ s^{-1}$]
k : thermal conductivity [$W\ m^{-1}\ K^{-1}$]
m : exponent of Re
M : mass flow rate [$kg\ s^{-1}$]
n : exponent of Pr
Nu : Nusselt number
Q : heat transfer rate [W]
Pr : Prandtl number
r : radius of a tube [m]
R_{foul} : fouling factor [$K\ m^2\ W^{-1}$]
Re : Reynolds number
t : thickness of a tube [m]
T : temperature [K]
U : overall heat transfer coefficient [$W\ m^{-2}\ K^{-1}$]
w : half length of the fin between tubes [m]

Δy : length of a control volume [m]

Greek

ε : emissivity
σ : Stefan-Boltzmann coefficient

Subscript

avg : average of inflow and outflow
conv : convection
CV : control volume
g : gas
h : hydraulic
i : inner wall of a tube
in : inflow of a control volume
inner : inner coil of a channel
j : gas or particle streams
o : outer wall of a tube
out : outflow of a control volume
outer : outer coil of a channel
p : particle
rad : radiation
ref : reference temperature (273.15 K)
steam : water/steam in the helical coil and membrane tube
tube : tube material
w : wall

REFERENCES

1. K. Park, D. Shin, G. Lee and E. S. Yoon, *Korean J. Chem. Eng.*, **29**, 1129 (2012).
2. C. Higman, *State of the gasification industry-the updated worldwide gasification database, Gasification Technologies Conf.*, Colorado Springs, CO, USA, Oct. 16 (2013).
3. R. Fernando, *Coal gasification*, CCC/140, IEA Clean Coal Centre (2008).
4. J. Ni, G. Yu, Q. Guo, Q. Liang and Z. Zhou, *Ind. Eng. Chem. Res.*, **49**, 4452 (2010).
5. J. Ni, G. Yu, Q. Guo, Z. Dai and F. Wang, *Chem. Eng. Sci.*, **66**, 448 (2011).
6. E. Martelli, T. Kreutz, M. Carbo, S. Consonni and D. Jansen, *Appl. Energy*, **88**, 3978 (2011).
7. Z. Yang, Y. Liu and Z. Cao, *Int. J. Chem. React. Eng.*, **9**, A85 (2011).
8. C. Higman and M. van der Burgt, *Gasification*, 2nd Ed., Gulf Professional Publishing, Oxford, UK (2008).
9. C. Botero, R. P. Field, R. D. Brasington, H. J. Herzog and A. F. Ghoniem, *Ind. Eng. Chem. Res.*, **51**, 11778 (2012).
10. G. Yu, J. Ni, Q. Liang, Q. Guo and Z. Zhou, *Ind. Eng. Chem. Res.*, **48**, 10094 (2009).
11. I.-S. Ye, S. Park, C. Ryu and S. K. Park, *Appl. Therm. Eng.*, **58**, 11 (2013).
12. S. Park, I.-S. Ye, J. Oh, C. Ryu and J. H. Koo, *Appl. Therm. Eng.*, Submitted (2014).
13. V. Gnielinski, *Heat transfer and pressure drop in helically coiled tubes, Proc. 8th Int. Heat Transfer Conf.*, **6**, 2847 (1986).
14. Z. Yang, Z. Zhao, Y. Liu, Y. Chang and Z.Cao, *Exp. Therm. Fluid Sci.*, **35**, 1427 (2011).
15. Z. Zhao, X. Wang, D. Che and Z. Cao, *Int. Comm. Heat Mass.*, **38**, 1189 (2011).
16. A. Zbogar, F. J. Frandsen, P. A. Jensen and P. Glarborg, *Prog. Energy Combust. Sci.*, **31**, 371 (2005).
17. K. C. Mills and J. M. Rhine, *Fuel*, **68**, 904 (1989).
18. T.-H. Shih, W. W. Liou, A. Shabbir, Z. Yang and J. Zhu, *Comput. Fluids*, **24**, 227 (1995).
19. T. F. Smith, Z. F. Shen and J. N. Friedman, *J. Heat Trans.*, **104**, 602 (1982).
20. ANSYS Inc., *ANSYS FLUENT 13 User's Guide*, Nov., Canonsburg, PA, USA (2010).
21. B. D. Bowen, M. Fournier and J. R. Grace, *Int. J. Heat Mass Trans.*, **34**, 1043 (1991).

Supporting Information

Modeling and analysis of a syngas cooler with concentric evaporator channels in a coal gasification process

Junho Oh*, In-Soo Ye*, Sangbin Park*, Changkook Ryu*,†, and Sung Ku Park**

*School of Mechanical Engineering, Sungkyunkwan University, Suwon 440-746, Korea
**Coal Conversion System Development Team, Corporate R&D Institute,
Doosan Heavy Industries & Construction, Daejeon, 305-811, Korea
(*Received 6 April 2014 • accepted 12 June 2014*)

EVALUATION OF OVERALL HEAT TRANSFER COEFFICIENT

If the helical coil has identical heat flux from the upper and lower quarters, the centerline becomes adiabatic. In contrast, the membrane water-wall has one side almost insulated by the pressure vessel filled with steam. CFD simulations were carried out to determine accurate values of overall heat transfer coefficient ($U_{gas\text{-}steam}$) for various input parameters. The number of quadrilateral cells was 5,428 in the 2-dimensional mesh. ANSYS Fluent (version 6.3) was used for the simulations varying the thermal conductivities and the fin lengths.

Fig. S2 illustrates the temperature profile in the helical coil and the membrane wall with an indicative condition. The heat transfer rate to the upper quarter of the helical coil was 3,783 W. Therefore, $U_{gas\text{-}steam}A_w=Q/(T_{gas}-T_{steam})$ became 12.61 W/K. On the other hand, the overall heat transfer coefficient of the helical coil was simplified into Eq. (9):

$$U_{gas\text{-}steam}=\frac{\pi/(2r_o+2w)}{1/h_{steam}r_i+\ln(r_o/r_i)/k_{tube}+R_{foul}+1/(h_{conv}+h_{rad})} \quad (9)$$

For the tube geometry with $R_{foul}=0$, $U_{gas\text{-}steam}A_w$ was calculated to be

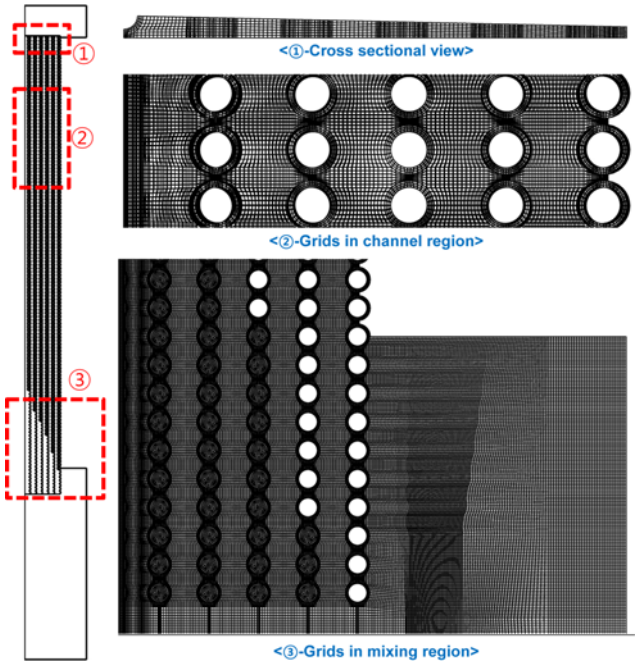

Fig. S1. Detailed image of the mesh for CFD.

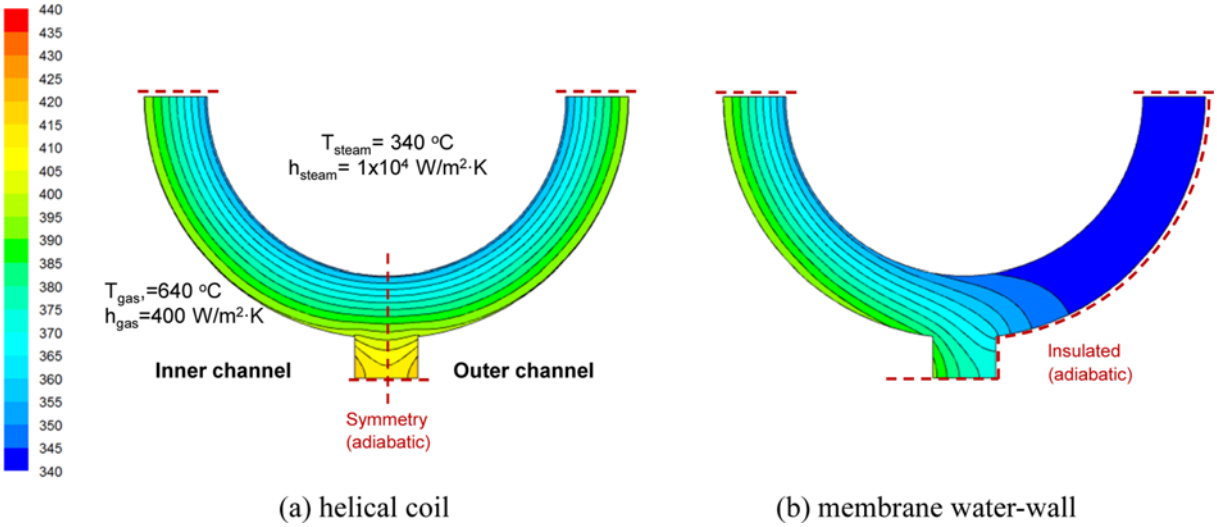

Fig. S2. Temperature profiles in a helical coil (a) and membrane water-wall (b) predicted by CFD under indicative conditions (T_{gas}=640 °C, T_{steam}=340 °C, h_{gas}=400 W/m²·K, h_{steam}=10,000 W/m²·K, k_{tube}=17 W/m·K, r_o=24.3 mm, w=4 mm).

12.46 W/K. Therefore, the equation underpredicted $U_{gas\text{-}steam}$ by 1.2%. The error increased slightly to 1.7% when k_{tube} became 40 W/m·K. Eq. (9) was also used for the membrane wall and the innermost coil in which one side faced the pressure vessel and the stagnant gas region, respectively. In this case, the lower quarter in Fig. S2(b) becomes an additional path for the heat transfer. The heat transfer rate to the steam through the half of the inner tube surface was 3,860 W, which was 76 W (1.98%) larger than the quarter of the helical coil. Therefore, the error involved in using Eq. (9) became 3.2%. Compared to other simplifications adopted, the errors in Eq. (9) were acceptable for the process model. Note that the same equations were used to derive h_{conv} from the CFD results and, therefore, the correlation of Nu partially compensated the errors involved in Eq. (9).